

Guozhen CHEN, Pinkuan LIU, Han DING

Structural parameter design method for a fast-steering mirror based on a closed-loop bandwidth

© The Author(s) 2019. This article is published with open access at link.springer.com and journal.hep.com.cn

Abstract When a fast-steering mirror (FSM) system is designed, satisfying the performance requirements before fabrication and assembly is vital. This study proposes a structural parameter design approach for an FSM system based on the quantitative analysis of the required closed-loop bandwidth. First, the open-loop transfer function of the FSM system is derived. In accordance with the transfer function, the notch filter and proportional-integral (PI) feedback controller are designed as a closed-loop controller. The gains of the PI controller are determined by maximizing the closed-loop bandwidth while ensuring the robustness of the system. Then, the two unknown variables of rotational radius and stiffness in the open-loop transfer function are optimized, considering the bandwidth as a constraint condition. Finally, the structural parameters of the stage are determined on the basis of the optimized results of rotational radius and stiffness. Simulations are conducted to verify the theoretical analysis. A prototype of the FSM system is fabricated, and corresponding experimental tests are conducted. Experimental results indicate that the bandwidth of the proposed FSM system is 117.6 Hz, which satisfies the minimum bandwidth requirement of 100 Hz.

Keywords fast-steering mirror, structural parameter, PI controller, bandwidth, notch filter

1 Introduction

A fast-steering mirror (FSM) is a rotational positioning stage that plays an important role in optical beam control systems to achieve pointing, tracking, and acquisition [1].

FSMs have been widely used in many fields, such as imaging [2,3] and laser processing systems [4], free-space optical communications [5,6], and laser weaponry [7,8]. With a high bandwidth, FSMs are capable of fast response and good disturbance rejection [9]. However, a high bandwidth typically requires a rigid elastic support [10,11]. A large actuator output force, which is costly and difficult to implement, is desirable for certain strokes. Moreover, the FSM is generally designed for a target application for which the bandwidth requirement is specific. If the FSM's structural parameters are poorly designed, the final bandwidth may fail to satisfy the practical requirements of the target application. Therefore, developing a structural parameter design approach, which can ensure that the FSM can satisfy the bandwidth requirement for a given target application, is crucial.

Many design approaches have been developed to achieve this goal. Kluk et al. [9] and Csencsics et al. [12] designed FSM mechanical systems, ensuring low stiffness in the motion direction to enable a large travel range and placing structural mode well above the crossover frequency to maximize the bandwidth. Yuan et al. [13] determined the structural parameters of an FSM by setting the designed stroke slightly larger than what was required and making the resonant frequency coincide with the expectation. However, mechanical structures in these studies were designed on the basis of the qualitative analysis of the open-loop frequency characteristic. Whether or not resultant FSMs satisfy the bandwidth requirement remains unknown until they are fabricated and assembled. In contrast to the aforementioned open-loop approach, Lu et al. [11] developed an FSM system based on the desired closed-loop bandwidth. However, the suspension mode frequency was simply set to be 0.25–0.5 times of the closed-loop bandwidth. Given that the final bandwidth is affected by the structure, load, and closed-loop control strategy, this design approach is inaccurate. Thus, designing FSM systems based on the quantitative analysis of the required closed-loop bandwidth is rare.

As can be inferred from previous strategies aimed at

Received April 5, 2019; accepted May 4, 2019

Guozhen CHEN, Pinkuan LIU (✉), Han DING
School of Mechanical Engineering, Shanghai Jiao Tong University,
Shanghai 200240, China
E-mail: pkliu@sjtu.edu.cn

addressing bandwidth challenges, the two major determinants of final bandwidth are the open-loop transfer function of the stage and the corresponding closed-loop control strategy. The open-loop transfer function is determined by the structural parameters and load of the stage. As the resonant modes substantially limit bandwidth, the control strategy is developed to eliminate vibration effects [14]. Effective methods to eliminate resonant modes mainly include the notch filter [15,16] and feedforward [17,18], input shaping [19], and integral resonant controllers [20]. Feedback controllers are designed to compensate for modeling uncertainties and disturbance. The proportional-integral (PI) controller is widely used as a feedback controller owing to its robustness to modeling errors and simplicity of implementation [21]. Therefore, to conduct the quantitative analysis of the bandwidth, the open-loop transfer function, resonant modes' damping methods, and feedback controller should all be considered.

In this study, a novel approach to the FSM system design is proposed. Structural parameters are designed on the basis of the quantitative analysis of the required closed-loop bandwidth. The bandwidth is derived from the theoretical analysis, with consideration of the open-loop transfer function and the closed-loop control strategy. With the bandwidth considered a constraint condition, structural parameters of the FSM are optimized to ensure that the final system can satisfy the bandwidth requirement. The rest of this paper is organized as follows: Section 2 presents the mechanical design of the FSM; Section 3 presents the open-loop transfer function of the stage and the closed-loop control strategy; Section 4 determines the structural parameters; Sections 5 and 6 detail the conducted simulations and experimental testing, respectively; finally, Section 7 concludes the study.

2 Mechanical design

In this study, the proposed FSM is applied in a laser weapon system to compensate for base vibration. The vibration of the base has low frequency (usually less than 100 Hz) and large magnitude. Therefore, the required bandwidth of the proposed FSM system is set at 100 Hz. The corresponding elliptical mirror has the dimensions $\text{Ø}100 \text{ mm} \times \text{Ø}70.7 \text{ mm} \times 15 \text{ mm}$ (long axis \times short axis \times height). The mechanical structure is composed of a mirror, a monolithic compliant mechanism (MCM), and a base, as shown in Fig. 1. The connected link is designed to connect the MCM and the voice coil actuator (VCA). The stage consists of four VCAs, with two sets of two VCAs arranged in a push-pull configuration to rotate the stage. The MCM is composed of a rigid frame and four elastic kinematic chains, as shown in Fig. 2(a). The elastic kinematic chain is composed of four translational plates, a rotational plate, and a decoupled plate, as shown in

Fig. 2(b). The translational plate is designed to achieve large translational motion along the z -axis. The rotational plate is designed to convert the translational motion of the VCA into the rotational motion of the FSM. The decoupled plate is used to minimize the transverse displacement of the coil and avoid any undesirable contact between the stator and the coil [22].

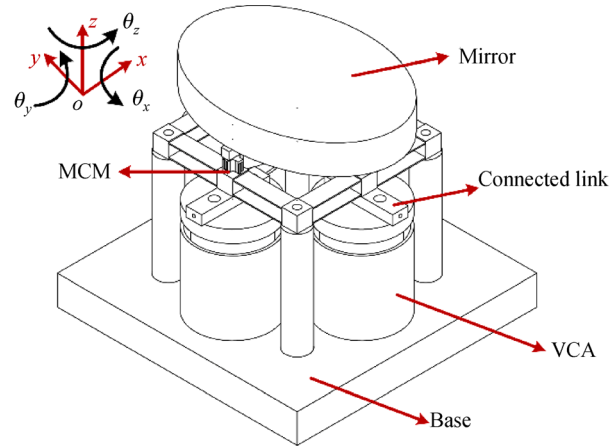


Fig. 1 Mechanical design of the FSM. MCM: Monolithic compliant mechanism; VCA: Voice coil actuator.

3 Transfer function of the FSM

Given that the mirror is elliptical, the inertial moment along θ_x -axis is larger than that along θ_y -axis, as shown in Fig. 1. When the same control strategy is applied, the bandwidth of the θ_x -axis is smaller than that of the θ_y -axis. Therefore, a theoretical analysis is conducted to study the characteristics of the θ_x -axis.

3.1 Open-loop transfer function of the stage

To achieve closed-loop control, deriving the transfer function of the FSM is necessary [23]. The Laplace transform of the dynamic model of the FSM is written as follows:

$$2rk_i i(s) - K\theta(s) = s^2 J\theta(s), \quad (1)$$

where s denotes the Laplace operator, r and K denote the rotational radius and the rotational stiffness of the FSM, respectively, k_i and i denote the force constant of the VCA and the current of the coil, respectively, and J and θ denote the inertial moment and rotational angle of the FSM, respectively.

According to Lagrange's equation, the inertial moment of the stage is written as follows:

$$J = 2r^2(m_1 + m_2) + J_1, \quad (2)$$

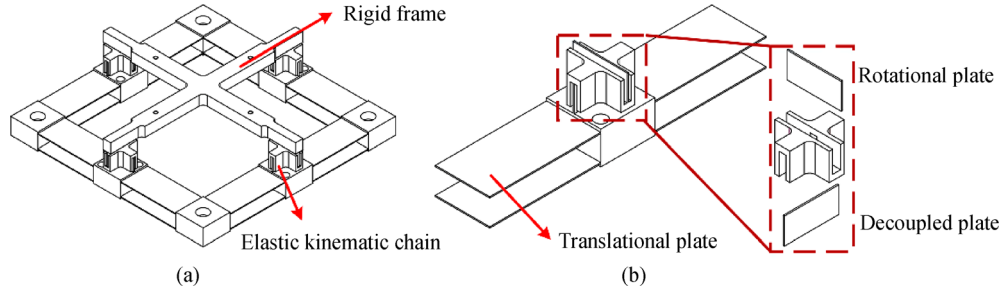


Fig. 2 (a) Monolithic compliant mechanism; (b) elastic kinematic chain.

where m_1 and m_2 denote the mass of the VCA and connected link, respectively, and J_1 denotes the inertial moment of the mirror.

The function of the electrical model of the VCA is derived from Kirchhoff's law. The corresponding Laplace transform is written as follows:

$$U(s) = (R + Ls)i(s) + k_i r \theta(s), \quad (3)$$

where U denotes the input voltage of the VCA, and R and L are the resistance and inductance of the VCA, respectively.

In accordance with Eqs. (1)–(3), the transfer function ($G(s)$) of the FSM is derived as follows:

$$G(s) = \frac{\theta(s)}{U(s)} = \frac{20.2r}{B_1 s^3 + B_2 s^2 + B_3 s + 10.1K}, \quad (4)$$

where

$$B_1 = 4.26 \times 10^{-4} r^2 + 6.62 \times 10^{-7},$$

$$B_2 = 1.16 r^2 + 1.81 \times 10^{-3},$$

$$B_3 = 204.02 r^2 + 3.7 \times 10^{-3} K.$$

3.2 Closed-loop control strategy

As shown in Fig. 3, the closed-loop control system is composed of the notch filter, PI controller and the transfer function of the FSM.

As discussed in Section 3.1, the open-loop transfer function of the FSM is a third-order system, which contains a second-order oscillation link and a first-order inertial link. The resonant modes with low damping ratio result in low gain margins that limit the application of the high-gain feedback controllers [16]. Thus, a notch filter is generally used to suppress resonant behavior to improve the high-bandwidth performance of the closed-loop system. The transfer function of the notch filter ($N(s)$) is

defined as follows [21]:

$$N(s) = \frac{s^2 + 2\zeta\omega_0 s + \omega_0^2}{s^2 + 2\omega_0 s + \omega_0^2}, \quad (5)$$

where ζ and ω_0 denote the damping ratio and the resonance frequency of the second-order oscillation link, respectively.

A PI controller is widely used due to its robustness to modeling errors and simplicity of implementation. The PI controller transfer function ($C(s)$) is written as follows:

$$C(s) = k_p + \frac{k_i}{s}, \quad (6)$$

where k_p and k_i denote proportional gain and integral gain, respectively.

3.3 Calculation of the bandwidth

As the open-loop transfer function of the FSM and corresponding notch filter are determined, the bandwidth of the closed-loop control system depends on the design of the PI controller. Given that the bandwidth varies substantially according to the chosen parameters of the PI controller, obtaining the optimal parameters of the PI controller is necessary to maximize the bandwidth.

The optimization process is conducted under two constraint conditions. First, the gain and phase margins are set to be larger than 3 and 60° , respectively, to guarantee the robustness of the system [24,25]. Second, the settling time (2% tolerance) is set to be less than 20 ms to guarantee the time domain performance. Then, the maximum bandwidth of the closed-loop control system can be obtained using the iteration method. The method is explained as follows: k_p and k_i are increased incrementally until the stability margin of the closed-loop control system is out of scope. Various values for k_p and k_i , which satisfy

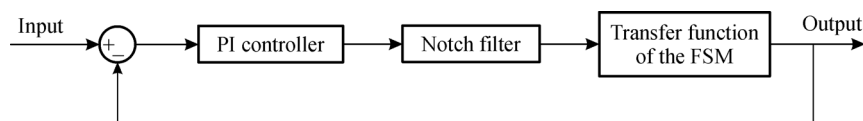


Fig. 3 Block diagram of the closed-loop control system.

the two constraint conditions, are obtained, and the corresponding closed-loop bandwidth is calculated using MATLAB software. Thus, the maximum bandwidth with optimal parameters for the PI controller can be obtained. The process is shown in Fig. 4.

4 Design of structural parameters

4.1 Determination of rotational radius and stiffness

As discussed in Section 3.1, two variables (stiffness K and rotational radius r) are unknown in the open-loop transfer function of the FSM. The effects of each variable on the bandwidth of the closed-loop control system are shown in Fig. 5.

The bandwidth increases with the increase in K (Fig. 5(a)), whereas the bandwidth decreases with the increase in r (Fig. 5(b)). Therefore, the bandwidth of the closed-loop control system can be improved by setting a relatively large K and relatively small r .

Parameters of variables r and K are obtained through an

optimization process. The constrained objective function is listed as follows:

1) The objective of optimization is to guarantee that the bandwidth of the closed-loop control system will be larger than 100 Hz.

2) Parameter ranges:

$25 \text{ mm} \leq r \leq 45 \text{ mm}$; $30 \text{ N} \cdot \text{m}/\text{rad} \leq K \leq 60 \text{ N} \cdot \text{m}/\text{rad}$.

The optimization results are shown as follows:

$$r = 33 \text{ mm}, K = 50 \text{ N} \cdot \text{m}/\text{rad}.$$

4.2 Static modeling

Analytical static modeling is conducted using the compliance matrix method to obtain the relationship between the structural parameters and rotational stiffness of the FSM [26,27]. For a flexure hinge, the compliance matrices in the coordinate frames $o_i\text{-}xyz$ and $o_j\text{-}xyz$ are C_i and C_j , respectively. The coordinate transformation can be written as

$$C_j = R_i(\theta)P(r_i)C_iP(r_i)^T R_i(\theta)^T, \quad (7)$$

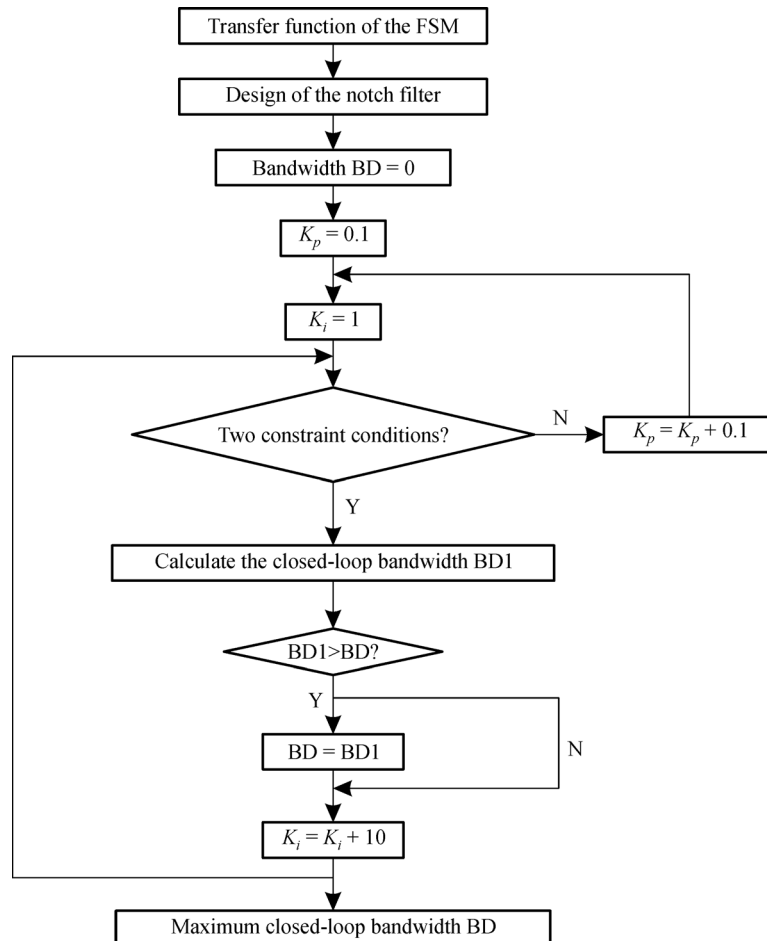


Fig. 4 Parameter optimization of the gains of the PI controller gains.

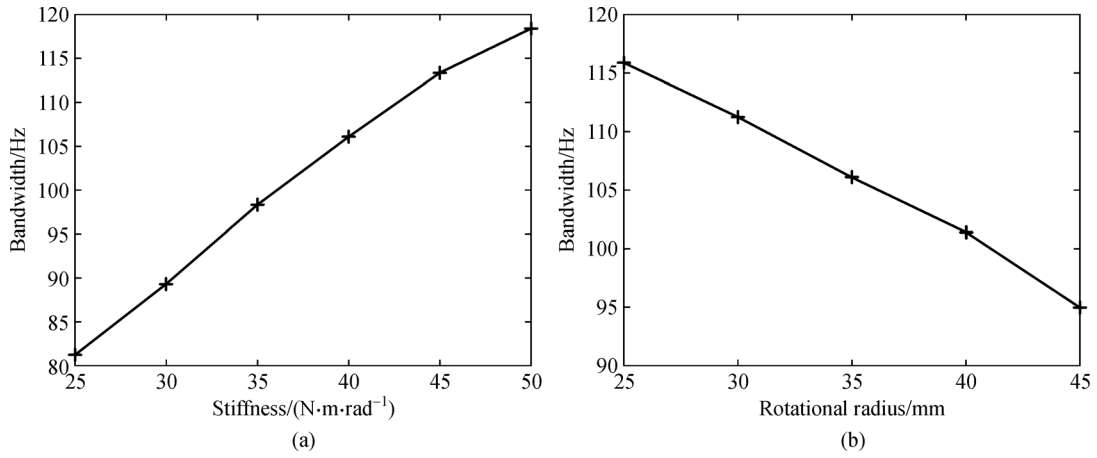


Fig. 5 Effects of variables on the bandwidth of the closed-loop control system. Effects of (a) rotational stiffness and (b) rotational radius.

where $\mathbf{P}(r_i)$ is the translational transformation matrix, $\mathbf{r}_i = [x, y, z]^T$ is the position coordinate of the point o_j in the reference frame $o_i\text{-}xyz$, $\mathbf{R}_i(\theta)$ is the rotational transformation matrix, and θ is the rotational angle about the i -axis.

As shown in Fig. 6, the compliance matrices of the translational and decoupled plates are defined as \mathbf{C}_1 and \mathbf{C}_2 in coordinate frames $o_t\text{-}xyz$ and $o_d\text{-}xyz$, respectively.

$$\mathbf{C}_1 = \begin{bmatrix} c_{11} & 0 & 0 & 0 & 0 & 0 \\ 0 & c_{12} & 0 & 0 & 0 & c_{13} \\ 0 & 0 & c_{14} & 0 & -c_{15} & 0 \\ 0 & 0 & 0 & c_{16} & 0 & 0 \\ 0 & 0 & -c_{15} & 0 & c_{17} & 0 \\ 0 & c_{13} & 0 & 0 & 0 & c_{18} \end{bmatrix}, \quad (8)$$

$$\mathbf{C}_2 = \begin{bmatrix} c_{21} & 0 & 0 & 0 & c_{22} & 0 \\ 0 & c_{23} & 0 & -c_{24} & 0 & 0 \\ 0 & 0 & c_{25} & 0 & 0 & 0 \\ 0 & -c_{24} & 0 & c_{26} & 0 & 0 \\ c_{22} & 0 & 0 & 0 & c_{27} & 0 \\ 0 & 0 & 0 & 0 & 0 & c_{28} \end{bmatrix}, \quad (9)$$

where $c_{11} = \frac{L_1}{Et_1 b_1}$, $c_{12} = \frac{4L_1^3}{Eb_1^3 t_1^3} + \frac{1.175L_1}{Gt_1 b_1}$, $c_{13} = \frac{6L_1^2}{Eb_1^3 t_1^3}$,
 $c_{14} = \frac{4L_1^3}{Eb_1 t_1^3} + \frac{1.175L_1}{Gt_1 b_1}$, $c_{15} = \frac{6L_1^2}{Eb_1 t_1^3}$, $c_{16} = \frac{L_1}{Gkb_1 t_1^3}$,
 $c_{17} = \frac{12L_1}{Eb_1 t_1^3}$, $c_{18} = \frac{12L_1}{Eb_1^3 t_1^3}$, $c_{21} = \frac{4L_2^3}{Eb_2^3 t_2^3} + \frac{1.175L_2}{Gt_2 b_2}$,
 $c_{22} = \frac{6L_2^2}{Eb_2^3 t_2^3}$, $c_{23} = \frac{4L_2^3}{Eb_2 t_2^3} + \frac{1.175L_2}{Gt_2 b_2}$, $c_{24} = \frac{6L_2^2}{Eb_2 t_2^3}$,

$c_{25} = \frac{L_2}{Et_2 b_2}$, $c_{26} = \frac{12L_2}{Eb_2 t_2^3}$, $c_{27} = \frac{12L_2}{Eb_2^3 t_2^3}$, and $c_{28} = \frac{L_2}{Gkb_2 t_2^3}$. Here, E is the Young's modulus, and G denotes the shear modulus.

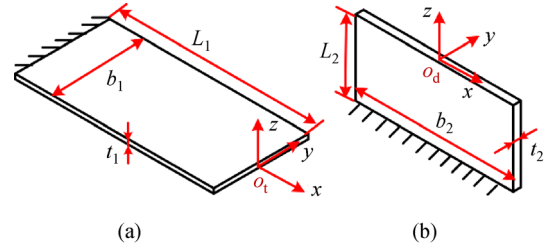


Fig. 6 Local coordinate frames of the (a) translational and (b) rotational plates.

The compound basic parallelogram mechanism (CBPM) is composed of four translational plates, which are defined as flexure hinge 1, 2, 3, and 4, as shown in Fig. 7(a). The compliance matrices of the four translational plates in coordinate frame $o_5\text{-}xyz$ are derived as follows:

$$\mathbf{C}_{o_1}^{o_5} = \mathbf{P}(r_1)\mathbf{C}_1\mathbf{P}(r_1)^T, \quad (10)$$

$$\begin{aligned} \mathbf{C}_{o_2}^{o_5} &= \mathbf{R}_x(\pi)\mathbf{C}_{o_1}^{o_5}\mathbf{R}_x(\pi)^T \\ &= \mathbf{R}_x(\pi)\mathbf{P}(r_1)\mathbf{C}_1\mathbf{P}(r_1)^T\mathbf{R}_x(\pi)^T, \end{aligned} \quad (11)$$

$$\begin{aligned} \mathbf{C}_{o_3}^{o_5} &= \mathbf{R}_z(\pi)\mathbf{C}_{o_1}^{o_5}\mathbf{R}_z(\pi)^T \\ &= \mathbf{R}_z(\pi)\mathbf{P}(r_1)\mathbf{C}_1\mathbf{P}(r_1)^T\mathbf{R}_z(\pi)^T, \end{aligned} \quad (12)$$

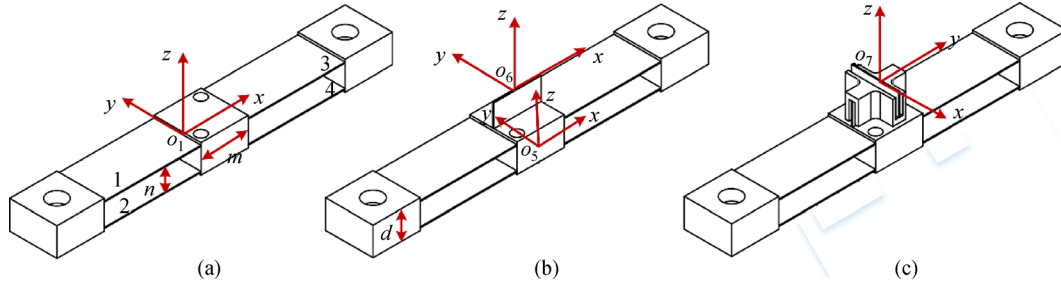


Fig. 7 Coordinate frames of the compliant mechanism.

$$\begin{aligned} \mathbf{C}_{o_4}^{o_5} &= \mathbf{R}_x(\pi) \mathbf{C}_{o_3}^{o_5} \mathbf{R}_x(\pi)^T \\ &= \mathbf{R}_x(\pi) \mathbf{R}_z(\pi) \mathbf{P}(\mathbf{r}_1) \mathbf{C}_1 \mathbf{P}(\mathbf{r}_1)^T \mathbf{R}_z(\pi)^T \mathbf{R}_x(\pi)^T, \end{aligned} \quad (13)$$

where $\mathbf{r}_1 = [m/2, 0, -n/2]^T$.

The four translational plates are arranged in parallel. Thus, the compliance matrix of the CBPM in the coordinate frame o_5 -xyz is written as follows:

$$\mathbf{C}_{o_5} = \left((\mathbf{C}_{o_1}^{o_5})^{-1} + (\mathbf{C}_{o_2}^{o_5})^{-1} + (\mathbf{C}_{o_3}^{o_5})^{-1} + (\mathbf{C}_{o_4}^{o_5})^{-1} \right)^{-1}. \quad (14)$$

The compliance matrix of the CBPM in the coordinate frame o -xyz is derived as follows:

$$\mathbf{C}_{o_5}^o = \mathbf{P}(\mathbf{r}_2) \mathbf{C}_{o_5} \mathbf{P}(\mathbf{r}_2)^T, \quad (15)$$

where $\mathbf{r}_2 = [0, (a+b)/2, h+c+d/2]^T$.

The compliance matrices of the rotational and decoupled plates in the coordinate frame o -xyz are derived as follows:

$$\mathbf{C}_{o_6}^o = \mathbf{P}(\mathbf{r}_3) \mathbf{C}_2 \mathbf{P}(\mathbf{r}_3)^T, \quad (16)$$

$$\mathbf{C}_{o_7}^o = \mathbf{R}_z\left(-\frac{\pi}{2}\right) \mathbf{P}(\mathbf{r}_4) \mathbf{C}_2 \mathbf{P}(\mathbf{r}_4)^T \mathbf{R}_z\left(-\frac{\pi}{2}\right)^T, \quad (17)$$

where $\mathbf{r}_3 = [0, (a+b)/2, c+h-L_2]^T$ and $\mathbf{r}_4 = [-(a+b)/2, 0, h]^T$.

Given that the CBPM, rotational plate, and decoupled plate are connected in series, the compliance matrix of the elastic kinematic chain can be written as follows:

$$\mathbf{C}_{o_a}^o = \mathbf{C}_{o_5}^o + \mathbf{C}_{o_6}^o + \mathbf{C}_{o_7}^o. \quad (18)$$

By rotating $\mathbf{C}_{o_a}^o$ $\frac{\pi}{2}$, π , and $-\frac{\pi}{2}$, the compliance matrices of the other three elastic kinematic chains can be written as follows:

$$\mathbf{C}_{o_b}^o = \mathbf{R}_z\left(\frac{\pi}{2}\right) \mathbf{C}_{o_a}^o \mathbf{R}_z\left(\frac{\pi}{2}\right)^T, \quad (19)$$

$$\mathbf{C}_{o_c}^o = \mathbf{R}_z(\pi) \mathbf{C}_{o_a}^o \mathbf{R}_z(\pi)^T, \quad (20)$$

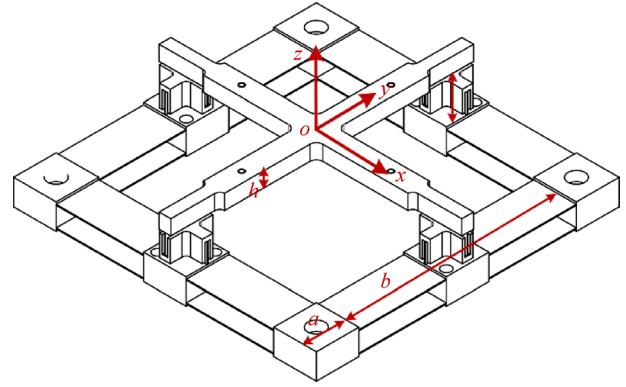


Fig. 8 Coordinate frame of the FSM.

$$\mathbf{C}_{o_d}^o = \mathbf{R}_z\left(-\frac{\pi}{2}\right) \mathbf{C}_{o_a}^o \mathbf{R}_z\left(-\frac{\pi}{2}\right)^T. \quad (21)$$

The four elastic kinematic chains are arranged in parallel, as shown in Fig. 8. Therefore, the compliance matrix of the FSM is derived as follows:

$$\mathbf{C}_o = (\mathbf{C}_{o_a}^o)^{-1} + (\mathbf{C}_{o_b}^o)^{-1} + (\mathbf{C}_{o_c}^o)^{-1} + (\mathbf{C}_{o_d}^o)^{-1})^{-1}. \quad (22)$$

The rotational stiffness of the FSM is written as follows:

$$K = \frac{1}{C_o(5,5)}. \quad (23)$$

4.3 Determination of structural parameters

In accordance with Section 4.1, the rotational radius and rotational stiffness of the FSM are set at 33 mm and 50 N·m/rad, respectively.

On the basis of Eq. (23), the structural parameters of the FSM are optimized based on three constraint conditions:

- 1) K is approximately equal to 50 N·m/rad;
- 2) $\frac{a+b}{2} = 33$ mm;
- 3) Range of parameters (unit: mm): $20 \leq L_1 \leq 35$, $4 \leq L_2 \leq 10$, $6 \leq b_1 = b_2 \leq 12$, $0.4 \leq t_1 \leq 0.6$, and $0.3 \leq t_2 \leq 0.6$.

The structural parameters optimization results are $L_1 =$

25 mm, $L_2 = 5$ mm, $b_1 = b_2 = 8$ mm, $t_1 = 0.52$ mm, and $t_2 = 0.42$ mm.

5 Simulation analyses

5.1 Stiffness of the FSM structure

The structural parameters of the FSM are derived from the theoretical calculation of rotational stiffness. Therefore, verifying the effectiveness of the static model is necessary. Finite element analysis is conducted using ANSYS Workbench software. The FSM structure is constructed from Al-7075. Forces are applied in a push-pull configuration. The deformation behavior is shown in Fig. 9. According to the finite element analysis, the rotational stiffness of the FSM is 49.58 N·m/rad. When this value is compared with the theoretical calculation (48.33 N·m/rad), the determined error is 2.52%, indicating the effectiveness of the static model.

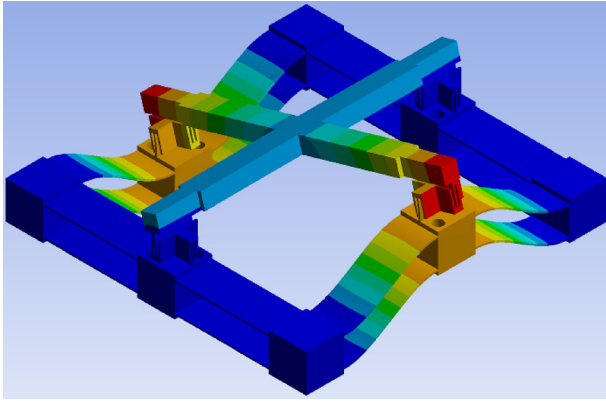


Fig. 9 Rotational motion of the FSM.

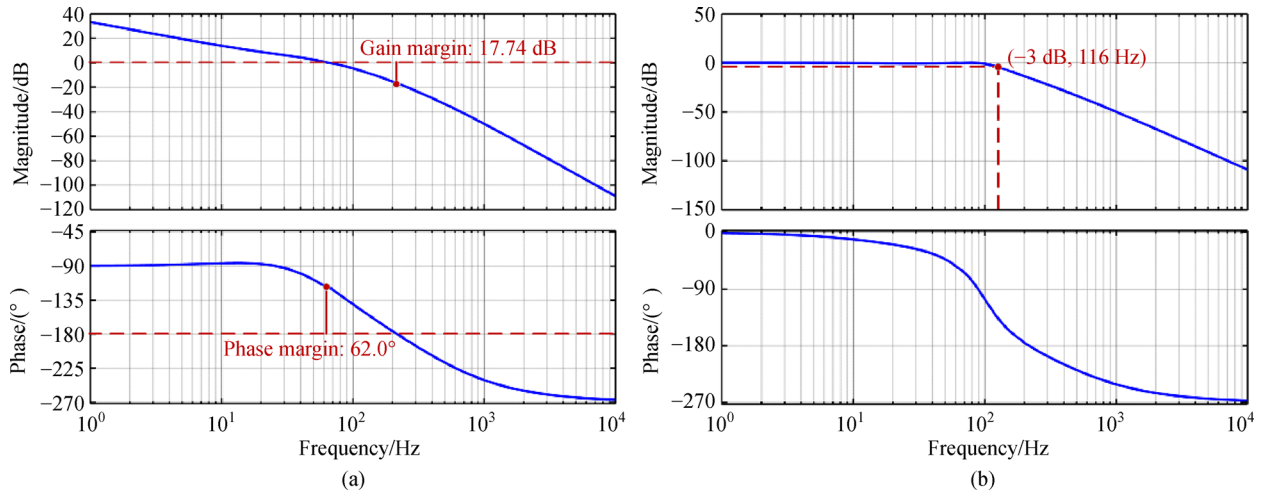


Fig. 10 Simulation results of (a) open-loop and (b) closed-loop frequency responses.

5.2 Bandwidth of the closed-loop control system

According to Section 4.3, the structural parameters of the FSM is determined. According to the simulation results, the variables for rotational radius r and stiffness K are 33 mm and 49.58 N·m/rad, respectively.

In accordance with Section 3.1, the open-loop transfer function of the FSM on the θ_x -axis is written as follows:

$$G(s) = \frac{5.92 \times 10^5}{s^3 + 2.73 \times 10^3 s^2 + 3.60 \times 10^5 s + 4.45 \times 10^8}. \quad (24)$$

In accordance with Section 3.2 and Section 3.3, the notch filter and PI controller are written as follows:

$$N(s) = \frac{s^2 + 72.46s + 1.67 \times 10^5}{s^2 + 817.32s + 1.67 \times 10^5}, \quad (25)$$

$$C(s) = 1480 + \frac{221501}{s}. \quad (26)$$

Frequency response characteristic analyses of the θ_x -axis are conducted using MATLAB. The open-loop frequency response characteristic is shown in Fig. 10(a). The magnitude and phase margins are 17.74 dB and 62°, respectively, indicating the robustness of the closed-loop system. The frequency response of the closed-loop system is shown in Fig. 10(b). The closed-loop bandwidth is 116 Hz, which exceeds the minimum bandwidth requirement of 100 Hz and thus more than satisfies the requirement.

6 Experimental tests

The compliant mechanism of the FSM is fabricated through a wire electrical discharge machining process. The VCAs (LVCA-038-038-01) are driven by two linear servo amplifiers (LA-210s-02-RA, VREDAN, Inc.). Two

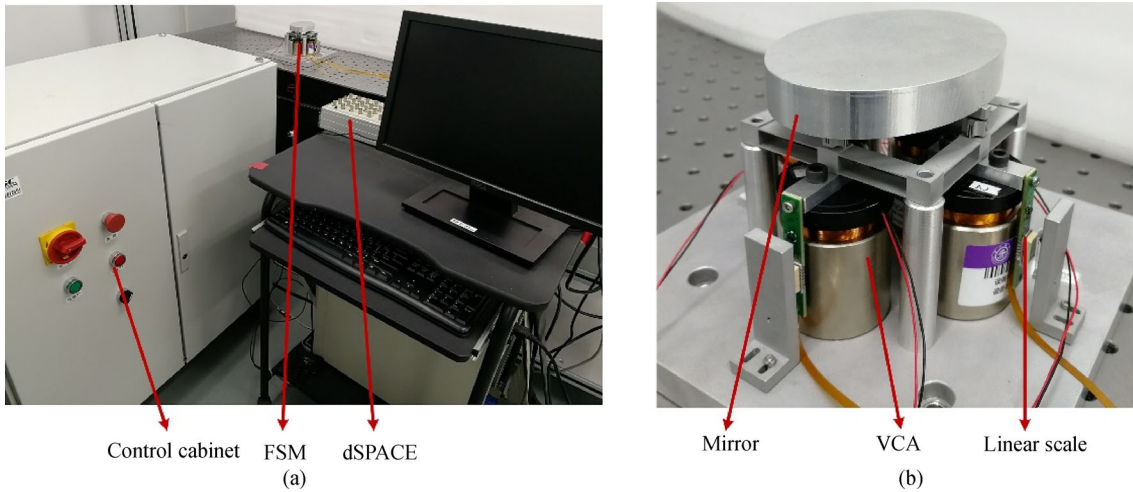


Fig. 11 Experimental setup of the stage: (a) Motion control system; (b) fast steering mirror stage.

linear scales (CE300-40, MicroE, Inc.) are used to measure the displacement, and the resolution is $1\ \mu\text{m}$. A Dspace-DS1103 is used to control the FSM system. The experimental stage is shown in Fig. 11.

6.1 Rotational stiffness

Different VCA forces are applied to the FSM, and corresponding displacements are measured using a linear scale. Force displacement tests are repeated thrice to reduce random errors. Experimental stiffness is obtained by linear fitting according to experimental test data. As shown in Fig. 12, stiffness around the x - and y -axes are 50.41 and $52.93\ \text{N}\cdot\text{m}/\text{rad}$, respectively. Compared with the theoretical calculation, the errors are 4.13% and 8.69% . These stiffness errors may be caused by a measurement error in the linear scale or a manufacturing error in the construction of the stage or a combination of both factors.

6.2 Closed-loop bandwidth

The frequency response of the stage is obtained by conducting system identification. A chirp signal is applied, and the output displacement of the stage is tested. The open-loop frequency response of the stage around the x -axis is shown in Fig. 13. The corresponding transfer function is calculated as follows:

$$G(s) = \frac{1.379 \times 10^9}{s^3 + 3491s^2 + 3.61 \times 10^5s + 5.862 \times 10^8}. \quad (27)$$

The damping ratio and resonance frequency are 0.0671 and $413.07\ \text{rad/s}$, respectively.

In accordance with Section 3.2, the notch filter is designed as follows:

$$N(s) = \frac{s^2 + 55.43s + 1.71 \times 10^5}{s^2 + 826.15s + 1.71 \times 10^5}. \quad (28)$$

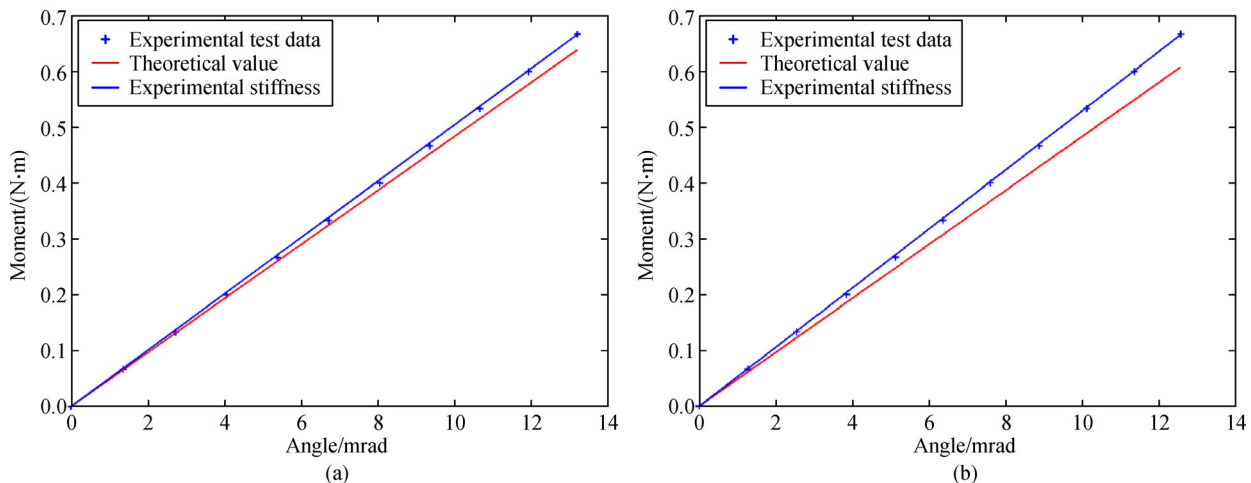


Fig. 12 Stiffness of the FSM around (a) x -axis and (b) y -axis.

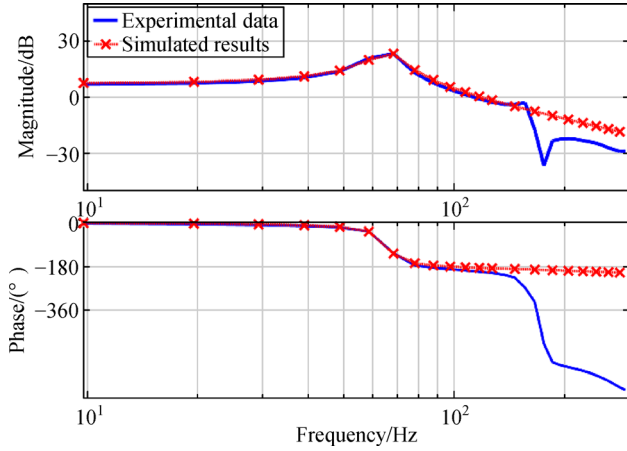


Fig. 13 Open-loop system identification of the FSM.

In accordance with Section 3.3, the gain parameters of the PI controller are obtained as follows:

$$k_p = 0.8, k_i = 131.$$

In consideration of the PI controller and notch filter, the

open-loop frequency response of the closed-loop control system in the θ_x -axis is shown in Fig. 14(a). The magnitude and phase margins are 8.06 dB and 65.2°, respectively. The closed-loop frequency response of the θ_x -axis are shown in Fig. 14(b). The bandwidth is 117.6 Hz. The experimental results are in good agreement with the theoretical analysis, verifying the effectiveness of the proposed structural parameter design method.

Similarly, the frequency response for the θ_y -axis is shown in Figs. 14(c) and 14(d). The gain and phase margins are 6.82 dB and 64.9°, respectively, whereas the bandwidth is 131.9 Hz. As such, the designed FSM system clearly satisfies the bandwidth requirement.

6.3 Motion characteristic test

The travel range and motion resolution of the stage are tested. The peak force of the applied VCA is 40.4 N. The characteristic of the peak force is intermittent due to heat generated in the coils. Thus, the current signal applied to the VCAs is a sinusoidal wave with a magnitude of 4 A. The sinusoidal signal responses are shown in Fig. 15. The

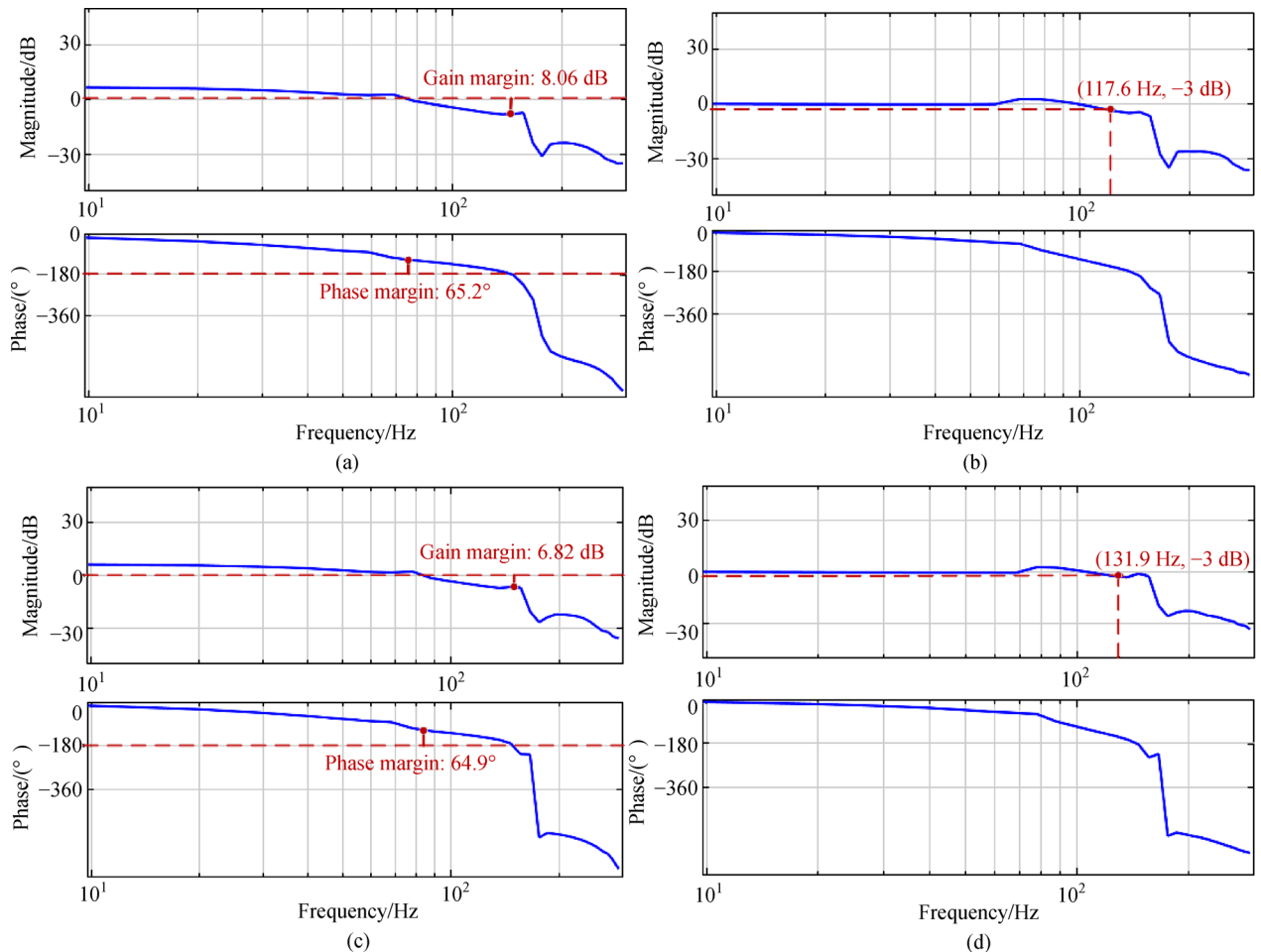


Fig. 14 Experimental results of the (a) open-loop frequency response around the x-axis; (b) closed-loop frequency response around the x-axis; (c) open-loop frequency response around the y-axis; (d) closed-loop frequency response around the y-axis.

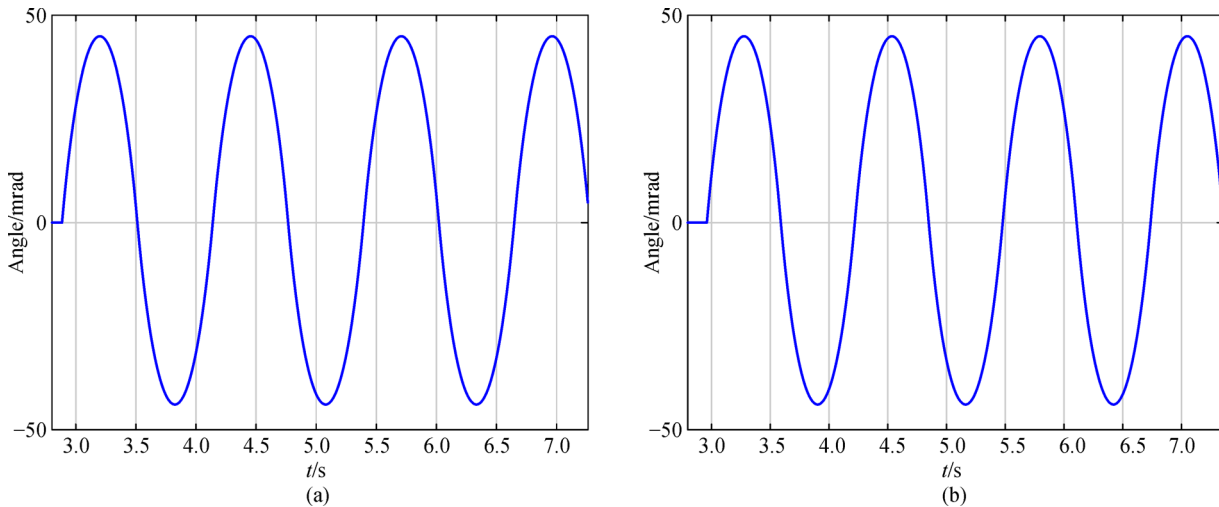


Fig. 15 Sinusoidal signal responses of the FSM around (a) the x - and (b) the y -axes.

maximum rotational angles of the FSM around the x - and the y -axes are ± 44.35 and ± 43.88 mrad, respectively.

The closed-loop control system includes the notch filter and PI feedback controller, as illustrated in Fig. 3. The motion resolution of the stage is tested by applying a consecutive step signal. As shown in Fig. 16, the resolution of the FSM is ± 0.03 mrad.

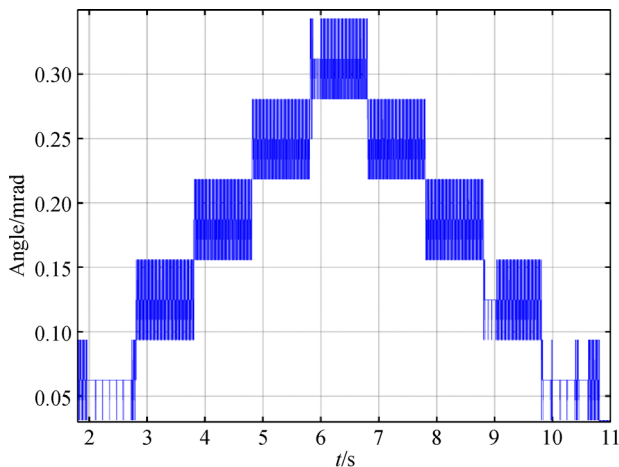


Fig. 16 Motion resolution of the FSM.

7 Conclusions

This study presents a structural parameter design method for an FSM system based on the required bandwidth. The closed-loop controller, including the notch filter and PI controller, is designed in accordance with the derived transfer function of the FSM. The two unknown variables (rotational radius r and stiffness K) in the transfer function are then optimized taking the bandwidth as a constraint condition. On the basis of the optimization results for r and K , the structural parameters of the FSM are determined.

Finally, simulations and experimental tests are conducted to verify the theoretical analysis, thus proving the efficacy of the proposed method.

Acknowledgements This work was supported by the Science Challenge Project (Grant No. JCKY2016212A506-0105).

Open Access This article is licensed under a Creative Commons Attribution 4.0 International License, which permits usage, sharing, adaptation, distribution, and reproduction in any medium or format, as long as you give appropriate credit to the original author(s) and the source, provide a link to the Creative Commons license, and indicate if changes were made.

Images and other third-party materials in this article are included in the article's Creative Commons license, unless indicated otherwise in a credit line to the material. If the material is not included in the article's Creative Commons license and your intended use is not permitted by statutory regulation or exceeds the permitted use, then you will need to obtain permission directly from the copyright holder.

To view a copy of this license, visit <http://creativecommons.org/licenses/by/4.0/>.

References

1. Loney G C. Design of a small-aperture steering mirror for high-bandwidth acquisition and tracking. *Optical Engineering*, 1990, 29(11): 1360–1365
2. Sun C, Ding Y, Wang D, et al. Backscanning step and stare imaging system with high frame rate and wide coverage. *Applied Optics*, 2015, 54(16): 4960–4965
3. Chen N, Potsaid B, Wen J T, et al. Modeling and control of a fast steering mirror in imaging applications. In: *Proceedings of IEEE International Conference on Automation Science and Engineering*. Toronto: IEEE, 2010, 27–32
4. Park J H, Lee H S, Lee J H, et al. Design of a piezoelectric-driven tilt mirror for a fast laser scanner. *Japanese Journal of Applied Physics*, 2012, 51(9S2): 09MD14
5. Liu W, Yao K, Huang D, et al. Performance evaluation of coherent free space optical communications with a double-stage fast-steering-

- mirror adaptive optics system depending on the Greenwood frequency. *Optics Express*, 2016, 24(12): 13288–13302
6. Wang C, Hu L, Xu H, et al. Wavefront detection method of a single-sensor based adaptive optics system. *Optics Express*, 2015, 23(16): 21403–21414
 7. Pan J W, Chu J, Zhuang S, et al. A new method for incoherent combining of far-field laser beams based on multiple faculae recognition. *Proceedings of SPIE 10710, Young Scientists Forum*, 2017, 1071034
 8. Wood G L, Perram G P, Marciniak M A, et al. High-energy laser weapons: Technology overview. *Proceedings of SPIE 5414, Laser Technologies for Defense and Security*, 2004, 1–25
 9. Kluk D J, Boulet M T, Trumper D L. A high-bandwidth, high-precision, two-axis steering mirror with moving iron actuator. *Mechatronics*, 2012, 22(3): 257–270
 10. Ito S, Schitter G. Atomic force microscopy capable of vibration isolation with low-stiffness Z-axis actuation. *Ultramicroscopy*, 2018, 186: 9–17
 11. Lu Y, Fan D, Zhang Z. Theoretical and experimental determination of bandwidth for a two-axis fast steering mirror. *Optik*, 2013, 124(16): 2443–2449
 12. Csencsics E, Schlarp J, Schitter G. High-performance hybrid-reluctance-force-based tip/tilt system: Design, control, and evaluation. *IEEE/ASME Transactions on Mechatronics*, 2018, 23(5): 2494–2502
 13. Yuan G, Wang D H, Li S D. Single piezoelectric ceramic stack actuator based fast steering mirror with fixed rotation axis and large excursion angle. *Sensors and Actuators. A, Physical*, 2015, 235: 292–299
 14. Gu G Y, Zhu L M, Su C Y, et al. Modeling and control of piezo-actuated nanopositioning stages: A survey. *IEEE Transactions on Automation Science and Engineering*, 2016, 13(1): 313–332
 15. Ling J, Feng Z, Ming M, et al. Damping controller design for nanopositioners: A hybrid reference model matching and virtual reference feedback tuning approach. *International Journal of Precision Engineering and Manufacturing*, 2018, 19(1): 13–22
 16. Wadikhaye S P, Yong Y K, Bhikkaji B, et al. Control of a piezoelectrically actuated high-speed serial-kinematic AFM nanopositioner. *Smart Materials and Structures*, 2014, 23(2): 025030
 17. Clayton G M, Tien S, Leang K K, et al. A review of feedforward control approaches in nanopositioning for high-speed SPM. *Journal of Dynamic Systems, Measurement, and Control*, 2009, 131(6): 061101
 18. Wang G, Chen G, Bai F. High-speed and precision control of a piezoelectric positioner with hysteresis, resonance and disturbance compensation. *Microsystem Technologies*, 2016, 22(10): 2499–2509
 19. Schitter G, Thurner P J, Hansma P K. Design and input-shaping control of a novel scanner for high-speed atomic force microscopy. *Mechatronics*, 2008, 18(5–6): 282–288
 20. Gu G Y, Zhu L M, Su C Y. Integral resonant damping for high-bandwidth control of piezoceramic stack actuators with asymmetric hysteresis nonlinearity. *Mechatronics*, 2014, 24(4): 367–375
 21. Gu G Y, Zhu L M. Motion control of piezoceramic actuators with creep, hysteresis and vibration compensation. *Sensors and Actuators A: Physical*, 2013, 197: 76–87
 22. Chen G, Ding Y, Zhu X, et al. Design and modeling of a compliant tip-tilt-piston micropositioning stage with a large rotation range. *Proceedings of the Institution of Mechanical Engineers, Part C: Journal of Mechanical Engineering Science*, 2018, 233(6): 2001–2014
 23. Wu X, Chen S, Chen W, et al. Large angle and high linearity two-dimensional laser scanner based on voice coil actuators. *Review of Scientific Instruments*, 2011, 82(10): 105103
 24. Ho W K, Hang C C, Zhou J H. Performance and gain and phase margins of well-known PI tuning formulas. *IEEE Transactions on Control Systems Technology*, 1995, 3(2): 245–248
 25. Paridari K, Tavazoei M S. Fractional PI tuning satisfying gain and phase margin constraints. In: *Proceedings of ASME 2011 International Design Engineering Technical Conferences and Computers and Information in Engineering Conference*, Volume 3: 2011 ASME/IEEE International Conference on Mechatronic and Embedded Systems and Applications, Parts A and B. Washington: ASME, 2011, 227–233
 26. Koseki Y, Tanikawa T, Koyachi N, et al. Kinematic analysis of a translational 3-d.o.f. micro-parallel mechanism using the matrix method. *Advanced Robotics*, 2002, 16(3): 251–264
 27. Liu H, Xie X, Tan R, et al. Mechatronic design of a novel linear compliant positioning stage with large travel range and high out-of-plane payload capacity. *Frontiers of Mechanical Engineering*, 2017, 12(2): 265–278